Crystal structures of human soluble adenylyl cyclase reveal mechanisms of catalysis and of its activation through bicarbonate

Silke Kleinboelting[a], Ana Diaz[b], Sebastien Moniot[a], Joop van den Heuvel[c], Michael Weyand[a], Lonny R. Levin[b], Jochen Buck[b], and Clemens Steegborn[a,1]

[a]Department of Biochemistry, University of Bayreuth, 95440 Bayreuth, Germany; [b]Department of Pharmacology, Weill Cornell Medical College, New York, NY 10065; and [c]Helmholtz-Zentrum für Infektionsforschung, 38124 Braunschweig, Germany

Edited by Carmen W. Dessauer, University of Texas Health Science Center at Houston, Houston, TX, and accepted by the Editorial Board January 24, 2014 (received for review December 6, 2013)

cAMP is an evolutionary conserved, prototypic second messenger regulating numerous cellular functions. In mammals, cAMP is synthesized by one of 10 homologous adenylyl cyclases (ACs): nine transmembrane enzymes and one soluble AC (sAC). Among these, only sAC is directly activated by bicarbonate (HCO_3^-); it thereby serves as a cellular sensor for HCO_3^-, carbon dioxide (CO_2), and pH in physiological functions, such as sperm activation, aqueous humor formation, and metabolic regulation. Here, we describe crystal structures of human sAC catalytic domains in the apo state and in complex with substrate analog, products, and regulators. The activator HCO_3^- binds adjacent to Arg176, which acts as a switch that enables formation of the catalytic cation sites. An anionic inhibitor, 4,4′-diisothiocyanatostilbene-2,2′-disulfonic acid, inhibits sAC through binding to the active site entrance, which blocks HCO_3^- activation through steric hindrance and trapping of the Arg176 side chain. Finally, product complexes reveal small, local rearrangements that facilitate catalysis. Our results provide a molecular mechanism for sAC catalysis and cellular HCO_3^- sensing and a basis for targeting this system with drugs.

activation mechanism | bicarbonate signaling | catalytic mechanism | inhibition mechanism

The ubiquitous second messenger cAMP regulates diverse physiological processes, from fungal virulence to mammalian brain function (1, 2). In mammals, cAMP can be generated by any of 10 differently expressed and regulated adenylyl cyclases (ACs): nine transmembrane enzymes (tmACs) and one soluble AC (sAC) (3). TmACs reside in the cell membrane, where they mediate cellular responses to hormones acting through G protein-coupled receptors (4). In contrast, sAC functions in various intracellular locations, providing cell-specific spatial and temporal patterns of cAMP (5–7) in response to intracellular signals, including calcium, ATP, and bicarbonate (HCO_3^-) (3, 8–10). HCO_3^- regulation of sAC enzymes is a direct effect on their catalytic domains and is conserved across bacterial, fungal, and animal kingdoms (1, 11–13). Via modulation of sAC, and sAC-like cyclase activities, HCO_3^- serves as an evolutionarily conserved signaling molecule mediating cellular responses to HCO_3^-, CO_2, and pH (3, 14). In mammals, sAC acts as a CO_2/HCO_3^-/pH sensor in processes such as sperm activation (15), acid-base homeostasis (16), and various metabolic responses (10, 17, 18). sAC has also been implicated in skin and prostate cancer and as a target for male contraceptives (19–21).

All mammalian ACs are class III nucleotidyl cyclases sharing homologous catalytic domains. Their catalytic cores are formed through symmetrical or pseudosymmetrical association of two identical or highly similar catalytic domains, C_1 and C_2 (22–24); in mammalian ACs, both domains reside on a single polypeptide chain. Such C_1C_2 pseudoheterodimers form two pseudosymmetrical sites at the dimer interface: the active site and a degenerated, inactive pocket (3, 23). A conserved Lys and an Asp/Thr in the active site recognize the base of the substrate ATP, and two conserved Asp residues bind two divalent cations, normally Mg^{2+} (23). The ions, called ion A and ion B, coordinate the substrate phosphates and support the intramolecular 3′-hydroxyl (3′-OH) attack at the α-phosphorous to form cAMP and pyrophosphate (PP_i) (3). In tmACs, the degenerate site binds forskolin (24), a plant diterpene that activates tmACs but has no effect on sAC (25). The forskolin activation mechanism and the existence of physiological ligands for this site in tmACs or in sAC remain unclear.

There are two sAC isoforms known to be generated by alternative splicing (26). Full-length sAC comprises N-terminal catalytic domains along with ∼1,100 residues with a little understood function except for an autoinhibitory motif and a heme-binding domain (3, 27, 28). Exclusion of exon 12 (26) generates a truncated isoform, sAC_t (residues 1–490), which comprises just the two sAC catalytic domains (sAC-cat) (25). sAC_t is widely expressed, and it is the isoform most extensively biochemically characterized (3, 8, 11). It is directly activated by Ca^{2+} and

Significance

Soluble adenylyl cyclase (sAC) generates the ubiquitous signaling molecule cAMP in response to bicarbonate. In physiological systems, bicarbonate is in nearly instantaneous equilibrium with carbon dioxide and pH; therefore, sAC, and its evolutionarily related cyclases, serve as nature's carbon dioxide/bicarbonate/pH sensors. In particular, bicarbonate regulation of mammalian sAC mediates numerous cellular processes, from sperm activation to pH homeostasis and mitochondrial ATP synthesis. We solved crystal structures of sAC's catalytic domains in complex with substrate, products, and regulators. The structures reveal insights into sAC catalysis, how bicarbonate binds to and activates sAC, and how sAC can be inhibited by a drug. Our results reveal mechanisms that will facilitate the development of drugs targeting this signaling system.

Author contributions: S.K., L.R.L., J.B., and C.S. designed research; S.K. and A.D. performed research; J.v.d.H. contributed new reagents/analytic tools; S.K., S.M., M.W., L.R.L., J.B., and C.S. analyzed data; and S.K., L.R.L., J.B., and C.S. wrote the paper.

Conflict of interest statement: J.B. and L.R.L. own equity interest in CEP Biotech, which has licensed commercialization of a panel of monoclonal antibodies directed against sAC.

This article is a PNAS Direct Submission. C.W.D. is a guest editor invited by the Editorial Board.

Data deposition: The atomic coordinates and diffraction data have been deposited with the Protein Data Bank, www.pdb.org: apo (PDB ID code 4CLF), soluble adenylyl cyclase (sAC)/α,β-methylene–ATP (ApCpp) (PDB ID code 4CLK), bicarbonate soak (PDB ID code 4CLL), biselenite soak (PDB ID code 4CLY), sAC/ApCpp bisulfite soak (PDB ID code 4CLW), apo bisulfite soak (PDB ID code 4CM2), apo ATP/$Mg2^+$ soak (PDB ID code 4CLU), apo cAMP soak (PDB ID code 4CLP), apo cAMP/pyrophosphate (PP_i) soak (PDB ID code 4CLT), apo 4,4′-diisothiocyanatostilbene-2,2′-disulfonic acid soak (PDB ID code 4CLZ), apo PP_i soak (PDB ID code 4CLS), and sAC/ApCpp bicarbonate soak (PDB ID code 4CM0).

[1]To whom correspondence should be addressed. E-mail: clemens.steegborn@uni-bayreuth.de.

This article contains supporting information online at www.pnas.org/lookup/suppl/doi:10.1073/pnas.1322778111/-/DCSupplemental.

HCO_3^-; Ca^{2+} supports substrate binding, and HCO_3^- increases turnover and relieves substrate inhibition (8), and this regulation is conserved in sAC-like enzymes from Cyanobacteria to humans (3, 13, 29). In a homodimeric, HCO_3^--regulated sAC homolog from *Spirulina platensis*, adenylyl cyclase C (CyaC), HCO_3^- appeared to facilitate an active site closure required for catalysis (13), but the HCO_3^- binding site and its mechanism of activation remained unknown.

Here, we present crystal structures of the human sAC-cat in apo form and in complex with substrate, products, bicarbonate, and a pharmacological inhibitor. The structures reveal insights into binding sites and mechanisms for sAC catalysis and for its regulation by physiological and pharmacological small molecules.

Results and Discussion

To identify its mechanism of activation by HCO_3^-, we produced human sAC-cat (residues 1–469) in insect cells and first crystallized the purified apo protein (30). Because molecular replacement phasing trials with class III AC structures failed, we solved the structure at a resolution of 1.7 Å through "single isomorphous replacement and anomalous scattering" (SIRAS) phasing using native and mercury derivative data (Table S1). The sAC-cat apo structure comprises two structurally similar domains, C_1 (residues 34–219) and C_2 (residues 288–463), with a central seven-stranded β-sheet shielded from solvent by helices (Fig. 1*A*; C_2 secondary structure elements underlined) consistent with known class III cyclase structures (23). C_1 and C_2 associate head to tail, resulting in a compact, pseudodimeric catalytic core. The 33 N-terminal residues form an extended tail (residues 1–12) and two helices (αN1 and αN2; Fig. 1*A*, *Right*), which form a death domain-like helix bundle along with two of the three α-helices within the ∼68-residue linker between C_1 and C_2. Three consecutive Pro residues (220–222) define the beginning of this linker; they are located at a corner of the core particle, close to a partially solvent-accessible hydrophobic patch formed by Ile88, Phe89/224/226/229/230, and Tyr240 (Fig. 1*B*). Poly-Pro stretches and hydrophobic surface areas are typically protein binding sites (31, 32), identifying this region as a potential interaction area for proteins or other sAC domains. In fact, in the crystal, part of this hydrophobic patch interacts with the extended N-terminal tail of a symmetry-related monomer (Fig. 1*B*), supporting its role in protein/domain interactions.

As in other class III ACs, two pseudosymmetrical sites are formed at the sAC pseudodimer interface. In the active site (Fig. 1*C*), most of the seven conserved catalytic residues are arranged similar to other class III AC structures (23). However, one of the two conserved Asp residues responsible for coordinating magnesium, Asp99, is shifted from the catalytic position (13, 24, 33) in apo sAC (Fig. 1*C*; CyaC Asp1061 is shown as a reference). An Asp rotation opening the ion sites was observed in the guanylyl cyclase (GC) Cya2 (22), but in sAC, the whole Asp99-containing β2/3 loop is pulled away, toward Arg176, through an Asp99/Arg176 salt bridge. Asp99 and the β2/3 loop are thereby held in an inactive position overlapping the ion site region. In tmAC, the pseudosymmetrical, degenerate site binds the activating diterpene forskolin. In apo sAC, a four-residue insertion in the C_2-β2/3 loop tightens the available space in this site compared with tmAC (Fig. 1*D*). This loop and the Arg176 side chain sterically prevent forskolin binding, explaining the insensitivity of sAC to this tmAC modulator (3, 25).

We next solved a structure of sAC-cat in complex with the ATP analog α,β-methylene–ATP (ApCpp). sAC was crystallized in the presence of $MgCl_2$, $CaCl_2$, and ApCpp, and the structure was solved through molecular replacement phasing with apo sAC-cat (Fig. 2*A* and Table S1). The structure was refined at a resolution of 2.2 Å, and the active site ligands, ATP analog and a divalent ion, were well defined by electron density (Fig. S1 *A* and *B*). Overall, the apo sAC structure and ATP analog complex are almost identical, but there are dramatic local rearrangements. The conserved ion-binding Asp47 tilts into position to form the ion sites and releases the Ser49 backbone, enabling an outward shift and partial unwinding of α1 starting immediately after Asp47 (Fig. 2*B*). Space to accommodate Asp47 and ions is provided through a flip of the β2/3 loop. It moves the second metal coordinating residue, Asp99, 4 Å away from Arg176, relieving their ionic interaction and positioning Asp99 for accommodating ions A/B and the associated ATP. The sAC-cat/ApCpp complex comprises only one metal ion, in position B, which supports substrate binding (3, 23). Coordination number and distances identify it as a Ca^{2+}, consistent with results on the cyanobacterial homolog CyaC and biochemical data showing that Ca^{2+} stimulates sAC activity by increasing substrate affinity (8, 13). In tmACs, a Ser (Ser1028 in rat tmACII-C_2) potentially contacts the ATP ribose ring oxygen (24, 33). In sAC and its homologs, the corresponding residue is Ala415 (Fig. 2*B*). Ala415 is unable to interact with the ribose oxygen, likely contributing to the lower apparent substrate affinity of sAC-like cyclases (K_m^{ATP} of ∼11 mM compared with <0.5 mM for tmACs). Ca^{2+} then increases the apparent substrate affinity (K_m^{ATP} of ∼1 mM) by providing a stronger interaction partner than Mg^{2+} for the ATP phosphates (13). In mammals, Ca^{2+}-dependent sAC activation is

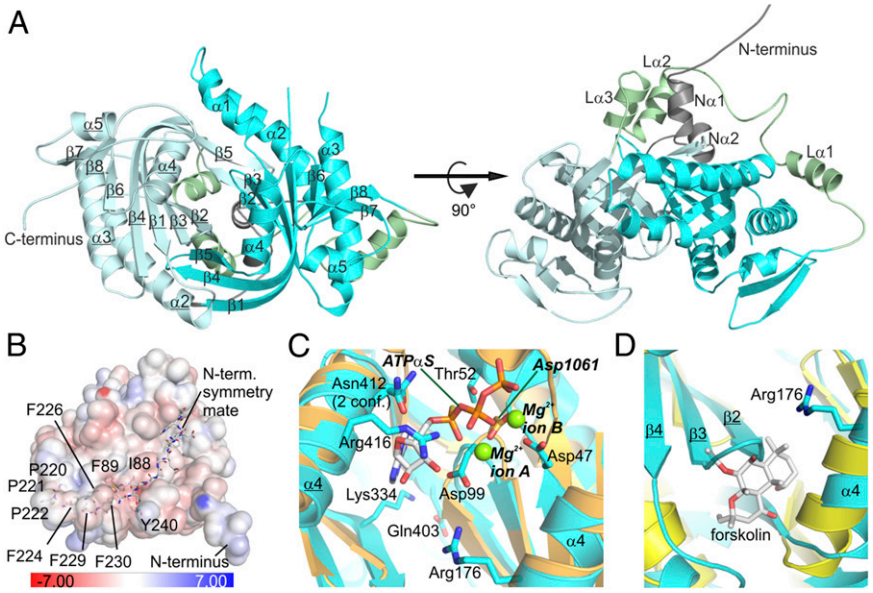

Fig. 1. Crystal structure of human sAC-cat apo enzyme. (*A*) Overall sAC-cat structure, with C_1 in cyan and C_2 in pale cyan and secondary structures labeled (C_2 labels underlined). (*Right*) This view highlights the N terminus (dark gray) and C_1-C_2 linker (green). (*B*) A sAC-cat apo surface region (colored according to electrostatic potential indicated in the scale bar) interacts with the N terminus of a symmetry mate (stick presentation). (*C*) An overlay of the active sites of sAC-cat apo (cyan; side chains colored according to atom type) and CyaC/ATPαS (orange; PDB ID code 1WC1) shows the overlap between human sAC Asp99 and ion site A (CyaC labels in italics). (*D*) Pseudosymmetrical sites of overlaid sAC-cat (cyan) and tmAC-C_1C_2 (yellow; PDB ID code 1AZS) structures, with the tmAC activator forskolin colored according to atom type.

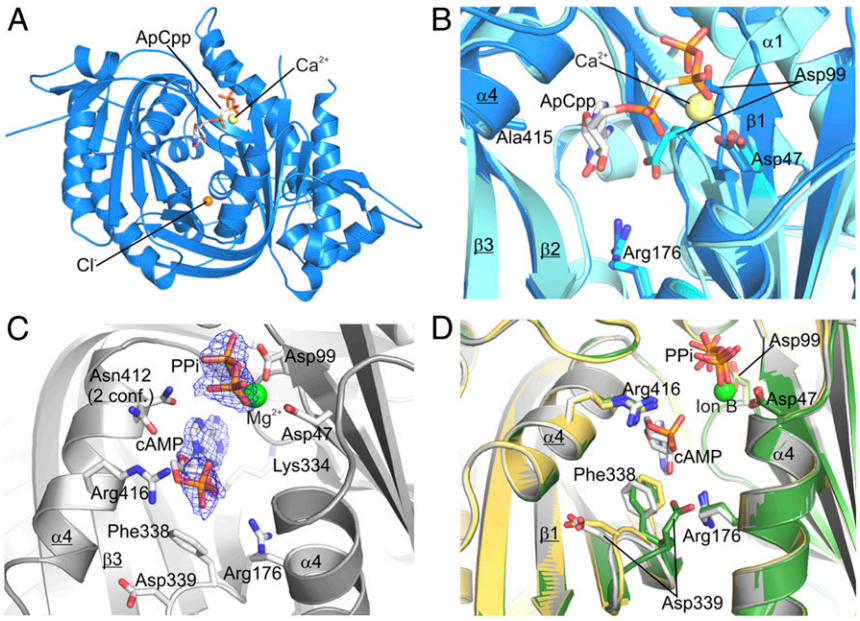

Fig. 2. Crystal structure of sAC-cat with bound ATP analog. (*A*) Overall structure of the sAC-cat/Ca^{2+}/ApCpp complex, with Ca^{2+} in yellow and ApCpp colored according to atom type. The chlorine in the pseudosymmetrical site is shown as an orange sphere. (*B*) Active site overlay of sAC-cat apo (cyan) and the ApCpp complex (blue), with relevant residues shown in stick presentation. (*C*) sAC product complex (cAMP, PP_i/Mg^{2+}) colored according to atom type and overlaid with $2F_o$-F_c density contoured at 1σ. (*D*) An overlay of the active sites of the sAC-cat complex with both products cAMP and PP_i (gray), the sAC-cat/PP_i complex resulting from soaking with PP_i (green), and the sAC-cat/PP_i complex resulting from soaking with ATP and substrate turnover (yellow) highlights the local rearrangement of the β2/β3 loop around Asp339.

physiologically relevant, for example, in insulin secretion (10, 17) and mitochondrial energy metabolism (34). The second ion, ion A, appears to bind transiently during catalysis to the ATP/metal B complex (13, 35), and the sAC-cat/Ca^{2+}/ApCpp complex has a water bound in this position.

In the sAC-cat/Ca^{2+}/ApCpp complex, Lys334, which is the conserved Lys in ACs distinguishing them from GCs by recognizing the ATP base (3), remains in its apo position, rotated away from the substrate site. It interacts with the Ade base only through a water molecule. Soaking apo sAC crystals with ATP/Mg^{2+} resulted in a 1.8-Å structure of a sAC/Mg^{2+}/PP_i complex (Fig. S1*C* and Table S2), showing that crystallized sAC-cat is catalytically active and that this Lys334 conformation is functional. Other AC/ATP-analog complexes show a Lys/Ade interaction (23), but with reaction-competent substrates, this interaction appears to form late during catalysis and is relevant for turnover rather than substrate binding (22, 36). The AC activity of sAC is inhibited by GTP (Fig. S1*D*) with a K_i of ∼1 mM (calculated based on competition), revealing that sAC binds GTP and ATP with comparable affinities and suggesting that it discriminates between the nucleotides only during turnover.

In our sAC/Ca^{2+}/ApCpp complex, the triphosphate assumes a conformation suitable for the inline reaction similar to the previously solved CyaC/ApCpp/metal complex (13). The γ-phosphate sits in a pocket at the α1 N terminus; the β-phosphate interacts with Lys144, which might act as a PP_i "receptor"; and the α-phosphate interacts with Arg416, which likely stabilizes the additional negative charge of the transition state. Finally, Arg176 is positioned next to the 3′-OH and might facilitate its deprotonation. To examine product interactions, we soaked apo crystals with the products PP_i and cAMP, alone or in combination, which yielded sAC-cat/cAMP (Fig. S1*E*), sAC-cat/PP_i (Fig. S1*F*), and sAC-cat/cAMP/PP_i (Fig. 2*C*) complexes (resolutions of 1.9 Å, 1.85 Å, and 1.95 Å, respectively; Tables S2 and S3). The sAC-cat/cAMP and sAC-cat/cAMP/PP_i structures represent previously unsolved complexes of an AC with cAMP. Comparison of these PP_i and cAMP complexes with sAC/ApCpp (Fig. S1*G*) reveals that nucleoside and β/γ-phosphates hardly shift, suggesting that the α-phosphate swings toward the 3′-OH for product formation. In the cAMP complexes (Fig. 2 *C* and *D*), Lys334 again interacts with the base via a water, consistent with the transient direct interaction proposed above. Interestingly, the two PP_i complexes, the sAC/Mg^{2+}/PP_i complex resulting from ATP turnover (ATP/Mg^{2+} soak, see above; Fig. S1*C*) and the sAC-cat/Mg^{2+}/PP_i complex resulting from soaking apo sAC with PP_i, are clearly distinct (Fig. 2*D*). Although divalent ion and PP_i occupy the same positions, Asp339 and the C_2-β2/3 loop are in the apo conformation (same as sAC/ApCpp conformation) in the PP_i soak but flip away from the active site in the complex, which resulted from ATP turnover. In this complex, the enzyme cyclized the soaked ATP into cAMP and PP_i but the cAMP was not retained due to its lower affinity (see below). The conformational change is also seen in the sAC/cAMP/PP_i complex that was formed by soaking with both products, cAMP and PP_i (Fig. 2*C*), but not in the complex with cAMP alone. Thus, the C_2-β2/3 loop flip only occurs in the presence of both products, suggesting that it reflects an intermediate catalytic state. Product release was speculated to be induced through a steric clash with Asn412 (23). In the sAC/cAMP/PP_i complex (Fig. 2*C*), this residue assumes two conformations, oriented toward PP_i as in the ApCpp complex and oriented toward the cAMP ring oxygen. It remains to be shown whether this change contributes to product formation or, more subtle than through steric overlap, to product release.

We next identified the activator binding site of sAC through soaking of apo sAC crystals with bicarbonate (resolution of 1.7 Å; Table S1). Excellent difference electron density adjacent to Val172 reveals that HCO_3^- binds between Lys95 and Arg176, almost coplanar with the Arg guanidinium group (Fig. 3 *A* and *B* and Fig. S2 *A* and *B*). The sAC/HCO_3^- complex confirms previous evidence that the bicarbonate anion, and not CO_2, directly stimulates sAC (11, 13, 29). Soaking apo sAC with biselenite or bisulfite (resolution of 2.05 Å and 1.8 Å, respectively; Tables S1 and S2), both of which structurally resemble HCO_3^- and could be located unambiguously by their anomalous scattering signal (Fig. S2 *C* and *D*), identified the same site, confirming it as the bicarbonate binding site (BBS). This region corresponds to the entrance of the degenerate site, which accommodates forskolin in tmACs. Its identification as the BBS confirms speculations that the degenerate site accommodates physiological regulators and communicates with the active site (3). Presumably, this degenerated site with regulatory function represents an evolutionary remnant from homodimeric ancestor class III cyclases that can show cooperativity or half-of-the-site activity (22, 37).

Bicarbonate binding leaves the overall sAC structure unchanged, but an increased frequency of multiple side chain conformations suggests there may have been a "loosening" of the protein conformation, enabling catalytic motions. Upon activator binding, the Arg176 side chain tilts toward the HCO_3^-, and it no longer traps Asp99 and the β2/β3 loop (Fig. 3*B*). The β2/β3 loop moves into

a substrate binding-competent conformation, similar to the sAC/ApCpp complex; however, Asp99 is left in an "open" state, where ion sites are accessible but still require further rotation of the Asp side chain for binding (Fig. 3*B*). The sAC/HCO_3^- complex suggests that the Arg176 side chain performs a key function in HCO_3^- activation, acting as a lever connecting regulatory and active sites. Lys95, in contrast, remains unchanged upon HCO_3^- binding but may contribute to regulation as a positively charged HCO_3^- docking spot. We tested these roles by determining the HCO_3^- potencies on sAC-cat variants with Arg176 and Lys95 mutated to Ala (individually and in concert). Arg176Ala showed significantly decreased sensitivity for the activator, with the EC_{50} elevated to >30 mM compared with 12 mM for WT sAC (Fig. 3*C*), consistent with its role as a lever connecting regulatory and active sites. The Lys95Ala mutant exhibited diminished specific activity in the presence of Mg-ATP, suggesting it plays additional roles in catalysis, but it also showed decreased HCO_3^- affinity (EC_{50} = 19 mM), consistent with its role in coordinating HCO_3^-. As expected, the Lys95Ala/Arg176Ala double mutant, which disrupted both HCO_3^- interacting side chains, showed no detectable HCO_3^- activation (no EC_{50} could be determined; Fig. 3*C*). Bisulfite and biselenite, whose geometry differs slightly from HCO_3^-, do not activate the enzyme (Fig. S2*E*). Both bind in the BBS slightly differently from HCO_3^- (Fig. S2 *C* and *D*), and neither triggered release of the Arg176 lever (Fig. 3*D*), supporting that its rearrangement mediates activation. Other anions can occupy the BBS without triggering the Arg176 lever. In apo sAC, an acetate from the crystallization solution was bound in the BBS, whereas in sAC/ApCpp crystals, a strong spherical density observed next to Arg176 was modeled as a chloride anion (Fig. 2*A*) based on signal strength and crystallization drop content. High concentrations of chloride and acetate did not stimulate sAC but showed weak interference with sAC activation by HCO_3^- (Fig. S2*E*). Thus, of the BBS-binding anions tested, only HCO_3^- stimulates sAC activity and triggers release of the Arg176 lever and formation of the open state of the cation sites.

In contrast to the stable HCO_3^- complex obtained with apo sAC crystals, soaking the sAC/ApCpp crystals with HCO_3^- decreased diffraction power and resulted in an unchanged complex, with ApCpp and Cl^-, but not HCO_3^-, bound in the active site and BBS and with Arg176 in the nonactivated conformation (Table S3). In contrast, soaking sAC/ApCpp crystals with bisulfite, which did not induce the Arg176 side-chain shift in apo sAC, resulted in well-defined additional density in the sAC/ApCpp complex (Fig. 3*E*); thus, nonactivating ligands can still occupy the BBS in the presence of substrate. This observation indicates that activator binding in the presence of substrate involves a protein conformation not compatible with the packing of our crystals, and we even conjecture that activator and substrate do not form stable complexes with sAC concomitantly. We rather speculate that (*i*) bicarbonate binds before the substrate, preparing the active site for productive ATP binding, and/or (*ii*) bicarbonate binding to the enzyme/substrate complex supports turnover and possibly product release. Active site preparation for productive ATP binding could explain how HCO_3^- relieves substrate inhibition (8). In this model, substrate binding might expel the activator, which would explain the relatively low affinity of HCO_3^-, a feature required due to its high physiological concentrations. Binding measurements in presence of Ca^{2+}, which does not support sAC activity in absence of Mg^{2+}, show that HCO_3^- increases the ATP affinity of sAC-cat (Fig. 3*F*), consistent with the activator supporting substrate binding by enabling ion site formation. In addition to the Arg176 flip toward HCO_3^- in apo sAC, HCO_3^- induces Phe338 to insert into a pocket formed by Met300/419 (Fig. S2*F*). This conformational change widens the active site entrance, which could also facilitate substrate binding. The fact that HCO_3^- increases V_{max} while leaving K_m unchanged (8) would be consistent with a catalytic substrate distortion, already predicted to be responsible for discrimination between ATP and GTP, if the distortion starts during binding. Indeed, HCO_3^- increased the affinity for cAMP while decreasing the affinity for PP_i (Fig. 3*F*), suggesting HCO_3^- changes binding of the adenosine and PP_i moieties. Such changes would be expected if substrate stretching supports cAMP/PP_i separation. Alternatively, the activator could stimulate turnover and/or product release after substrate binding. The loss in diffraction power for sAC/ApCpp upon HCO_3^- soaking might suggest a function in turnover but could also be a nonspecific effect, and the diminished PP_i affinity in presence of HCO_3^- (Fig. 3*F*) would support a model where the activator facilitates product release. This model is most consistent with previous kinetic data suggesting PP_i release as a potential rate-limiting step in tmACs (38), and with our observation that only PP_i was retained in the active site when sAC-cat apo crystals were soaked with ATP/Mg^{2+}. The models may not be mutually exclusive; bicarbonate may bind before the substrate to prepare for productive ATP binding and also after the substrate to support catalysis and PP_i release.

Pharmacological sAC modulation has potential therapeutic applications (19–21, 39), and because artificially manipulating the natural activator bicarbonate is problematic in physiological systems, sAC-selective modulators would facilitate in vivo studies. In tmAC, the space corresponding to the hydrophilic sAC BBS between Arg176 (Asn in tmAC) and Lys95 is blocked by a hydrophobic residue (Leu438 in tmACV-C_1, interacting with Phe338). Such molecular differences result in a shifted, larger, and more hydrophobic tmAC site accommodating forskolin (Fig. 1*D*), and although the BBS should also allow targeting sAC with specific drugs, it appears to be too small for typical drug-like

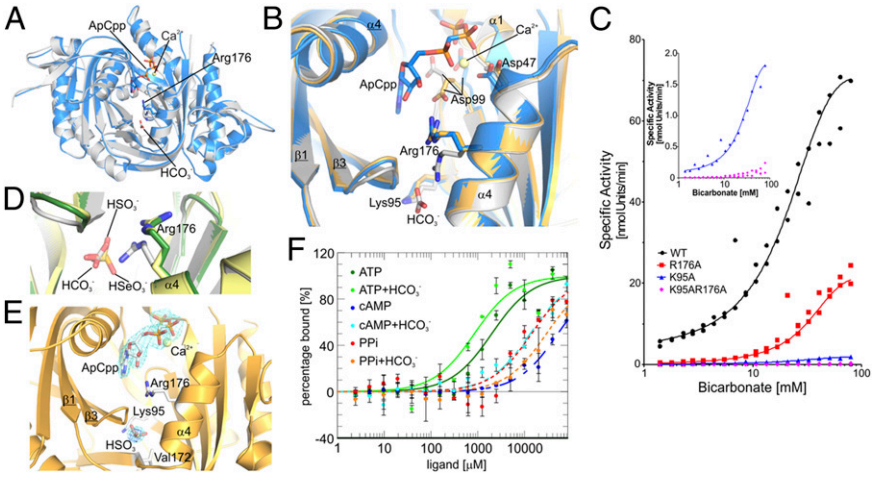

Fig. 3. sAC-cat activation by bicarbonate. (*A*) Overall structure of the sAC-cat bicarbonate complex (gray), overlaid with the sAC-cat/ApCpp complex (blue). Ligands are shown as sticks (ApCpp, bicarbonate) or as a sphere (Ca^{2+}). (*B*) Overlay of active site regions of apo sAC (yellow), sAC/ApCpp (blue), and the sAC/bicarbonate complex (gray) shows the HCO_3^--triggered Arg176 movement. (*C*) HCO_3^- concentration–response for AC activity of WT human sAC-cat (black dots) and for the mutants R176A (red squares), K95A (blue triangles), and K95A/R176A (magenta diamonds). (*Inset*) Data for K95A and K95AR176A with an expanded *y* axis. (*D*) Overlay of the regulatory sites of sAC shows the different geometries and binding details of HCO_3^- (gray), HSO_3^- (green), and $HSeO_3^-$ (yellow) and illustrates the Arg176 movement uniquely triggered by HCO_3^-. Ligands are shown as sticks colored according to atom type. (*E*) sAC/ApCpp complex with bisulfite bound in the regulatory site, overlaid with $2F_o$-F_c density (1σ; cyan) and anomalous scattering density (3σ; blue). (*F*) Binding affinity to sAC-cat for ATP (K_d = 2.0 ± 0.4 mM), cAMP (K_d = 54.2 ± 13.4 mM), and PP_i (K_d = 14.2 ± 0.3 mM). Addition of 50 mM HCO_3^- changed the K_d for ATP (0.9 ± 0.1 mM), cAMP (18.6 ± 6.1 mM), and PP_i (30.7 ± 12.1 mM). Error bars indicate SD (n = 2).

molecules. In an attempt to identify a pharmacological approach to exploit the sAC BBS, we therefore tested 4,4′-diisothiocyanatostilbene-2,2′-disulfonic acid (DIDS), which has effects on cellular HCO_3^-/pH systems normally attributed to inhibition of bicarbonate transporters (40). We speculated that DIDS's sulfonates might mimic HCO_3^- and allow inhibitory binding to BBS and additional regulatory site regions. DIDS indeed inhibited sAC in a dose-dependent manner, with an IC_{50} of 43 ± 6 μM (Fig. 4*A*). In the presence of HCO_3^-, the DIDS concentration–response was shifted to the right, resulting in a DIDS IC_{50} of 130 ± 9 μM in presence of 80 mM HCO_3^-, which shows that DIDS inhibition is indeed competitive with HCO_3^-. Soaking sAC-cat apo crystals with DIDS yielded strong difference density in three binding sites, which were all well modeled with the inhibitor (resolution of 1.9 Å; Fig. 4*B* and Table S3). Soaking at lower DIDS concentrations excluded a crystal contact site (labeled as III in Fig. 4*B*). Activity assays with varying ATP and DIDS concentrations showed competition between substrate and inhibitor (Fig. 4*C*), indicating that the internal DIDS site (labeled as I in Fig. 4*B*), blocking the active site entrance and overlapping with the ATP site, is relevant for inhibition (Fig. 4*D*). Although not reaching the BBS, the inhibitor blocks its access and traps the Arg176 side chain and the BBS-bound acetate (Fig. 4*E*). DIDS binds with its aromatic rings and stilbene unit to a hydrophobic cleft at the active site entrance formed by Phe296/336/338, Ala415, Leu345, and Val411 on one side and Phe45, Ala97/100, and Leu102 on the other side (Fig. 4*E*). The distortion of the DIDS aromatic rings from coplanarity might indicate a strained conformation, and thus potential for compound improvement. Electrostatic interactions to the sulfonyl groups are formed by Arg416 (4.8 Å) and Arg176 (3.8 Å); however, their interaction geometry does not yet appear optimal, and there are no specific H-bonds except to Asp339 (2.9 Å), again suggesting that the compound could be significantly improved. Interestingly, the sAC surface has mostly negative potential, except for the active site entrance environment (Fig. 4*F* and Fig. S3). This positive funnel likely supports binding of the anionic substrate ATP, and it could hinder PP_i release consistent with product release being rate-limiting (38). This charge distribution should also channel bicarbonate toward its binding site and guide DIDS to the enzyme's entrance, where it blocks access for substrate and activator (Fig. 4 *D* and *F*). These results reveal the sAC entrance region as a target site for pharmacological inhibition with hydrophobic/anionic compounds.

In summary, our results reveal the molecular structure of the human sAC catalytic core and its binding site for the activator bicarbonate, and they reveal insights into the sAC catalytic mechanism and how it can be regulated by physiological and pharmacological modulators.

Materials and Methods

Chemicals. All chemicals were obtained from Sigma if not stated differently.

Cloning, Recombinant Expression, and Purification of Human sAC Protein. For crystallization, sAC-cat was cloned in a baculovirus with C-terminal His-tag, expressed in the Helmholtz-Protein Sample Production Facility, and purified as described in detail elsewhere (30). Shortly, His-tagged sAC-cat was expressed in Hi5 cells and purified through nickel affinity, anion exchange, and size exclusion chromatography. For activity assays, either the His-tagged protein or a GST-tagged version was used. The GST construct was generated by cloning human sAC-cat (residues 1–469) in a baculovirus vector with N-terminal GST-tag. sAC-cat single-site variants were made with this construct using the QuikChange protocol. WT and mutant sAC-cat were expressed in Hi5 cells through infection for 48 h, followed by centrifugation at 5,000 × *g* for 15 min. Cells were lysed in 50 mM Tris (pH 7.5), 1 mM DTT, 150 mM NaCl, 10 μg/mL aprotinin/leupeptin, and 1 mM PMSF, and cytosol was generated at 50,000 × *g* for 30 min at 4 °C. The only AC activity remaining in the supernatant was due to the expressed sAC.

Crystallization and Structure Solution. sAC-cat was crystallized in its apo form in hanging drops at 4 °C with 500 μL as reservoir solution. Further details are described by Kleinboelting et al. (30). Crystals were cryoprotected through soaking in 100 mM sodium acetate (pH 4.8), 200 mM trisodium-citrate, 18% (wt/vol) PEG 4000, 20% (vol/vol) glycerol, and a complete diffraction dataset for an sAC-cat apo crystal in space group $P6_3$ was collected at 100 K at the Berlin Electron Storage Ring Society for Synchrotron Radiation synchrotron beamline 14.1 (BESSY BL14.1) operated by Helmholtz-Zentrum Berlin (41). All diffraction data were processed with X-ray Detector Software (XDS) (42) (Tables S1–S3). For phase determination, sAC-cat apo crystals were soaked with 0.05 mM thiomersal (5-h soak), 1 mM $HgCl_2$ (1-h soak), and 10 mM Pb (II)-acetate (24-h soak) under various conditions (compound concentration, soaking time) at 4 °C in cryoprotection solution, and a complete diffraction dataset was collected at BESSY BL14.1 at the absorption maximum of the respective heavy atom. Heavy atom sites were identified with Phenix-Hyss (43) for a mercury (two sites) and lead derivative (one site), respectively. The quality of single anomalous diffraction phases from either derivative was insufficient for model building, but using native data and the isomorphous mercury derivative dataset for SIRAS phasing in Phenix-Autosol resulted in excellent experimental phases. An incomplete initial sAC-cat model (395 residues) could be built automatically using the Phenix Autobuild option with an overall model map correlation of 81.8% and crystallographic and free residuals (R_{cryst} and R_{free}) values of 28% and 30%, respectively. Manual model building was done in Coot (44), and refinement was done in Refmac (45). Model quality was analyzed in Coot, and structure figures were generated in PyMOL (Schrödinger LLC). Electrostatic surfaces were calculated with the Adaptive Poisson–Boltzmann Solver algorithm (46) in PyMOL.

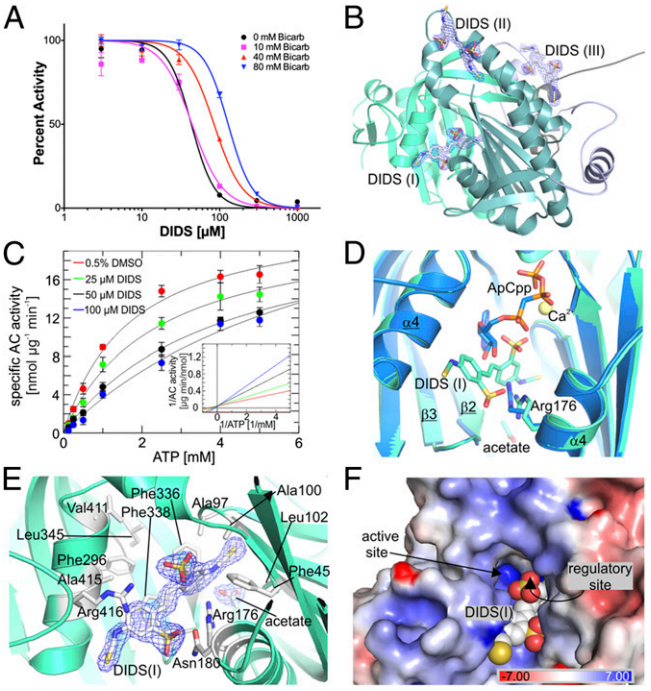

Fig. 4. sAC-cat inhibition by DIDS. (*A*) WT human sAC-cat activity assayed at the indicated concentrations of DIDS and in the presence of increasing amounts of HCO_3^-. DIDS IC_{50} determination in 0 mM HCO_3^- (IC_{50} 43 μM), in 10 mM HCO_3^- (44 μM), in 40 mM HCO_3^- (85 μM), and in 80 mM HCO_3^- (130 μM) is shown. Error bars indicate SD (n = 3). (*B*) Overall structure of sAC (C_1, teal; C_2, cyan; linker, blue) with all three DIDS molecules (sticks) overlaid with $2F_o$-F_c density (1σ). (*C*) sAC activity at various ATP and DIDS concentrations yields a constant V_{max} (24.6 ± 3.7 nmol·μg^{-1}·min^{-1}) and increasing apparent K_m values for ATP [0 μM DIDS (1.7 ± 0.3 mM), 25 μM DIDS (2.4 ± 0.4 mM), 50 μM DIDS (4.1 ± 0.5 mM), 100 μM DIDS (7.3 ± 2.7 mM)]. Error bars indicate SD (n = 2). (*Inset*) Lineweaver–Burk plot of the same data. (*D*) Overlay of the sAC-cat/DIDS structure (cyan) and the sAC/ApCpp complex (blue). (*E*) Details of the DIDS binding site in sAC show the interacting hydrophobic and positively charged residues (stick presentation) and the acetate trapped in the regulatory site. The $2F_o$-F_c density around the ligands is contoured at 1σ. (*F*) Protein surface of sAC-cat/DIDS colored according to electrostatic potential (indicated in scale bar), with DIDS (shown as spheres) partially blocking the active site entrance. Access to the regulatory site, behind the indicated DIDS sulfonyl group, is fully blocked.

To obtain an sAC-cat structure in complex with ATP analog, the protein was cocrystallized with 7.5 mM ApCpp in 100 mM phosphate/citrate (pH 4.2), 200 mM NaCl, and 24% (wt/vol) PEG 8000 seeded with apo sAC-cat crystals (1:1,000 dilution of a seed stock prepared by vortexing sAC apo crystals in reservoir solution) in a 1:2:3 ratio (seeding solution/reservoir/protein). For solving a structure of sAC-cat in complex with HCO_3^-, HSO_3^-, or $HSeO_3^-$, crystals were soaked with 40–60 mM of each substance for 4 h at 4 °C.

AC Assays. HPLC activity assays were done with 100 ng of purified, His-tagged sAC-cat in 50 mM Tris·HCl (pH 8.0), 50 mM NaCl, 10 mM $MgCl_2$, 10 mM $CaCl_2$, and 5 mM ATP at 37 °C. Reactions were stopped by flash-freezing and analyzed by reversed phase HPLC on a C18-column (3.5 μm, 4.6 × 50-mm XBridge columns; Waters) in 100 mM ammonium acetate (pH 8.8) and 10% (vol/vol) acetonitrile, with cAMP eluting after 6.6 min at a flow rate of 0.5 mL/min. Signal areas were integrated in LabSolutions software (Shimadzu). Measurements were done in duplicate, and data shown are representatives of at least two repetitions.

For the concentration–response experiments with bicarbonate and DIDS shown in Figs. 3*D* and 4*A*, GST-tagged sAC-cat lysate was used in a radioactivity-based assay in 50 mM Tris (pH 7.5) under the conditions indicated in a reaction containing ∼1,000,000 counts of α-^{32}P–labeled ATP as described previously (47). Generated cAMP was purified using sequential Dowex and Alumina chromatography as described previously (48).

Binding Measurements. Binding affinities to purified, His-tagged sAC-cats were determined by measuring microscale thermophoresis on a NanoTemper Monolith NT.label-free instrument (25% UV–light-emitting diode, 30% IR-laser power; NanoTemper Technologies). Assay buffer contained 50 mM Tris·HCl (pH 8), 50 mM NaCl, and 15 mM $CaCl_2$. K_d determinations were performed in duplicate. Binding transitions were fitted with a single-site equation in GraFit (Erithacus Software).

ACKNOWLEDGMENTS. We thank the BESSY staff for technical assistance. This study was supported by Deutsche Forschungsgemeinschaft Grants STE1701/1 and STE1701/11 (to C.S.) and National Institutes of Health Grants GM62328 and HD59913 (to L.R.L. and J.B.).

1. Hall RA, et al. (2010) CO(2) acts as a signalling molecule in populations of the fungal pathogen Candida albicans. *PLoS Pathog* 6(11):e1001193.
2. Hanoune J, Defer N (2001) Regulation and role of adenylyl cyclase isoforms. *Annu Rev Pharmacol Toxicol* 41:145–174.
3. Kamenetsky M, et al. (2006) Molecular details of cAMP generation in mammalian cells: A tale of two systems. *J Mol Biol* 362(4):623–639.
4. Sunahara RK, Taussig R (2002) Isoforms of mammalian adenylyl cyclase: Multiplicities of signaling. *Mol Interv* 2(3):168–184.
5. Zippin JH, et al. (2004) Bicarbonate-responsive "soluble" adenylyl cyclase defines a nuclear cAMP microdomain. *J Cell Biol* 164(4):527–534.
6. Acin-Perez R, et al. (2009) Cyclic AMP produced inside mitochondria regulates oxidative phosphorylation. *Cell Metab* 9(3):265–276.
7. Zaccolo M (2011) Spatial control of cAMP signalling in health and disease. *Curr Opin Pharmacol* 11(6):649–655.
8. Litvin TN, Kamenetsky M, Zarifyan A, Buck J, Levin LR (2003) Kinetic properties of "soluble" adenylyl cyclase. Synergism between calcium and bicarbonate. *J Biol Chem* 278(18):15922–15926.
9. Jaiswal BS, Conti M (2003) Calcium regulation of the soluble adenylyl cyclase expressed in mammalian spermatozoa. *Proc Natl Acad Sci USA* 100(19):10676–10681.
10. Zippin JH, et al. (2013) CO2/HCO3(-)- and calcium-regulated soluble adenylyl cyclase as a physiological ATP sensor. *J Biol Chem* 288(46):33283–33291.
11. Chen Y, et al. (2000) Soluble adenylyl cyclase as an evolutionarily conserved bicarbonate sensor. *Science* 289(5479):625–628.
12. Kobayashi M, Buck J, Levin LR (2004) Conservation of functional domain structure in bicarbonate-regulated "soluble" adenylyl cyclases in bacteria and eukaryotes. *Dev Genes Evol* 214(10):503–509.
13. Steegborn C, Litvin TN, Levin LR, Buck J, Wu H (2005) Bicarbonate activation of adenylyl cyclase via promotion of catalytic active site closure and metal recruitment. *Nat Struct Mol Biol* 12(1):32–37.
14. Tresguerres M, Buck J, Levin LR (2010) Physiological carbon dioxide, bicarbonate, and pH sensing. *Pflugers Arch* 460(6):953–964.
15. Esposito G, et al. (2004) Mice deficient for soluble adenylyl cyclase are infertile because of a severe sperm-motility defect. *Proc Natl Acad Sci USA* 101(9):2993–2998.
16. Pastor-Soler N, et al. (2003) Bicarbonate-regulated adenylyl cyclase (sAC) is a sensor that regulates pH-dependent V-ATPase recycling. *J Biol Chem* 278(49):49523–49529.
17. Ramos LS, Zippin JH, Kamenetsky M, Buck J, Levin LR (2008) Glucose and GLP-1 stimulate cAMP production via distinct adenylyl cyclases in INS-1E insulinoma cells. *J Gen Physiol* 132(3):329–338.
18. Tresguerres M, Levin LR, Buck J (2011) Intracellular cAMP signaling by soluble adenylyl cyclase. *Kidney Int* 79(12):1277–1288.
19. Flacke JP, et al. (2013) Type 10 soluble adenylyl cyclase is overexpressed in prostate carcinoma and controls proliferation of prostate cancer cells. *J Biol Chem* 288(5):3126–3135.
20. Zippin JH, Chadwick PA, Levin LR, Buck J, Magro CM (2010) Soluble adenylyl cyclase defines a nuclear cAMP microdomain in keratinocyte hyperproliferative skin diseases. *J Invest Dermatol* 130(5):1279–1287.
21. Pierre S, Eschenhagen T, Geisslinger G, Scholich K (2009) Capturing adenylyl cyclases as potential drug targets. *Nat Rev Drug Discov* 8(4):321–335.
22. Rauch A, Leipelt M, Russwurm M, Steegborn C (2008) Crystal structure of the guanylyl cyclase Cya2. *Proc Natl Acad Sci USA* 105(41):15720–15725.
23. Sinha SC, Sprang SR (2006) Structures, mechanism, regulation and evolution of class III nucleotidyl cyclases. *Rev Physiol Biochem Pharmacol* 157:105–140.
24. Tesmer JJ, Sunahara RK, Gilman AG, Sprang SR (1997) Crystal structure of the catalytic domains of adenylyl cyclase in a complex with Gsalpha.GTPgammaS. *Science* 278(5345):1907–1916.
25. Buck J, Sinclair ML, Schapal L, Cann MJ, Levin LR (1999) Cytosolic adenylyl cyclase defines a unique signaling molecule in mammals. *Proc Natl Acad Sci USA* 96(1):79–84.
26. Jaiswal BS, Conti M (2001) Identification and functional analysis of splice variants of the germ cell soluble adenylyl cyclase. *J Biol Chem* 276(34):31698–31708.
27. Chaloupka JA, Bullock SA, Iourgenko V, Levin LR, Buck J (2006) Autoinhibitory regulation of soluble adenylyl cyclase. *Mol Reprod Dev* 73(3):361–368.
28. Middelhaufe S, Leipelt M, Levin LR, Buck J, Steegborn C (2012) Identification of a haem domain in human soluble adenylate cyclase. *Biosci Rep* 32(5):491–499.
29. Cann MJ, Hammer A, Zhou J, Kanacher T (2003) A defined subset of adenylyl cyclases is regulated by bicarbonate ion. *J Biol Chem* 278(37):35033–35038.
30. Kleinboelting S, et al. (2013) Expression, purification, crystallization, and preliminary X-ray diffraction analysis of a mammalian type 10 adenylyl cyclase. *Acta Crystallogr Sect F Struct Biol Cryst Commun*, in press.
31. Saksela K, Permi P (2012) SH3 domain ligand binding: What's the consensus and where's the specificity? *FEBS Lett* 586(17):2609–2614.
32. Jones S (2012) Computational and structural characterisation of protein associations. *Adv Exp Med Biol* 747:42–54.
33. Tesmer JJ, et al. (1999) Two-metal-Ion catalysis in adenylyl cyclase. *Science* 285(5428):756–760.
34. Di Benedetto G, Scalzotto E, Mongillo M, Pozzan T (2013) Mitochondrial Ca^{2+} uptake induces cyclic AMP generation in the matrix and modulates organelle ATP levels. *Cell Metab* 17(6):965–975.
35. Garbers DL, Johnson RA (1975) Metal and metal-ATP interactions with brain and cardiac adenylate cyclases. *J Biol Chem* 250(21):8449–8456.
36. Mou TC, Masada N, Cooper DM, Sprang SR (2009) Structural basis for inhibition of mammalian adenylyl cyclase by calcium. *Biochemistry* 48(15):3387–3397.
37. Sinha SC, Wetterer M, Sprang SR, Schultz JE, Linder JU (2005) Origin of asymmetry in adenylyl cyclases: Structures of Mycobacterium tuberculosis Rv1900c. *EMBO J* 24(4):663–673.
38. Dessauer CW, Tesmer JJ, Sprang SR, Gilman AG (1999) The interactions of adenylate cyclases with P-site inhibitors. *Trends Pharmacol Sci* 20(5):205–210.
39. Schlicker C, et al. (2008) Structure-based development of novel adenylyl cyclase inhibitors. *J Med Chem* 51(15):4456–4464.
40. Boron WF (2001) Sodium-coupled bicarbonate transporters. *JOP* 2(4, Suppl):176–181.
41. Mueller U, et al. (2012) Facilities for macromolecular crystallography at the Helmholtz-Zentrum Berlin. *J Synchrotron Radiat* 19(Pt 3):442–449.
42. Kabsch W (2010) Xds. *Acta Crystallogr D Biol Crystallogr* 66(Pt 2):125–132.
43. Adams PD, et al. (2010) PHENIX: A comprehensive Python-based system for macromolecular structure solution. *Acta Crystallogr D Biol Crystallogr* 66(Pt 2):213–221.
44. Emsley P, Lohkamp B, Scott WG, Cowtan K (2010) Features and development of Coot. *Acta Crystallogr D Biol Crystallogr* 66(Pt 4):486–501.
45. Murshudov GN, Vagin AA, Dodson EJ (1997) Refinement of macromolecular structures by the maximum-likelihood method. *Acta Crystallogr D Biol Crystallogr* 53(Pt 3):240–255.
46. Baker NA, Sept D, Joseph S, Holst MJ, McCammon JA (2001) Electrostatics of nanosystems: Application to microtubules and the ribosome. *Proc Natl Acad Sci USA* 98(18):10037–10041.
47. Bitterman JL, Ramos-Espiritu L, Diaz A, Levin LR, Buck J (2013) Pharmacological distinction between soluble and transmembrane adenylyl cyclases. *J Pharmacol Exp Ther* 347(3):589–598.
48. Salomon Y (1979) Adenylate cyclase assay. *Adv Cyclic Nucleotide Res* 10:35–55.